Research Article

Investigation on a No Trial Weight Spray Online Dynamic Balancer

Xialun Yun [iD],[1,2,3] **Xuesong Mei** [iD],[1,2,3] **Gedong Jiang,**[1,2,3] **Zhenbang Hu,**[1,2,3] **and Zunhao Zhang**[1,2,3]

[1]*State Key Laboratory for Manufacturing Systems Engineering, Xi'an Jiaotong University, 710048 Xi'an, China*
[2]*Shaanxi Key Laboratory of Intelligent Robots, Xi'an Jiaotong University, 710049 Xi'an, China*
[3]*School of Mechanical Engineering, Xi'an Jiaotong University, Xi'an 710049, China*

Correspondence should be addressed to Xuesong Mei; xsmei@xjtu.edu.cn

In order to suppress the spindle vibration with high efficiency and high precision, a no without trial weight spray online balance method is proposed in this paper. By analyzing the relationship between the unbalanced excitation and the unbalanced response of the spindle, the relationship between the dynamic influence coefficient and the system model is studied. A high-speed spindle finite element analysis model was established, and the dynamic influence coefficient matrix was identified. A no trial weight spray online dynamic balancing system was developed, which has the advantages of without trial weight and high-precision loading. A new type of integrated balancing terminal that was formed using 3D printing technology was first proposed by our research group, and its advantages in various aspects are significantly higher than traditional assembly balanced terminals. The experimental verification of the without trial weight spray online dynamic balancing system was performed on a high-speed spindle test stand. Experiments show that the no trial weight spray online balancing method proposed in this paper can achieve high-efficiency and high-precision vibration suppression, greatly reducing balance time and cost of the spindle. At the same time, the online balance test also verified the reliability of the integrated balanced terminal.

1. Introduction

High-speed spindle is the core functional component of high-end CNC machine tools, and its dynamic characteristics will directly affect the machining level of machine tools. However, due to uneven material and manufacturing and assembly errors, the center of mass of the spindle and the center of rotation may be inconsistent. The unbalance of the spindle is inevitable. Unbalance can cause a disastrous accident in many engineering applications [1, 2]. Therefore, strict offline balancing will be performed when the spindle leaves the factory [3, 4]. However, the offline balance cannot compensate the unbalance mass caused by high-speed expansion, tool or grinding wheel wear, and the offline balance whose balance efficiency is low and requires the disassembly of the main shaft or grinding wheel. Therefore, it is very meaningful to study the high-speed and precision online dynamic balance [5, 6].

Spindle online balancing includes two main processes: (1) unbalanced vector identification and (2) vibration online suppression. A large number of researchers have studied the unbalanced vector identification method [7]. The unbalanced vector identification methods mainly include influence coefficient method (ICM) [8], modal balance method (MBM) [9], holospectral balance method (HBM) [10], and no trial weight balance method (NTWBM) [11]. Because NTWBM has the characteristics of without trial weight and high balancing precision, it has been widely applied in the intelligent spindle dynamic balancing [12, 13]. The research team headed by Mr. Qu Liang Sheng studied the no trial weight balancing method based on holospectral technique [14–16]. In 2009, Niebsch and Ramlau [17, 18] used wind turbines as the research object to study ill-conditioned phenomena in the inverse problem of the no trial weight balance method. Khulief et al. [19] and Li et al.

[20] simulated the functional expressions of the principal modes of the various stages of the rotor based on the finite element theory, and a good balancing effect is achieved. Research on spindle online vibration suppression technology began in the middle of the last century. Canadian scholars have proposed an active balancing device that is balanced by controlling the weight position. The mass block is driven by the motor [21]. Since then, many scholars have studied the way of changing the rotor mass distribution by balancing terminals. In 2006, Hredzak and Guo [22] developed an electromagnetic automatic balancing device. A movable electromagnetic adsorption device on the outside of the disc is used to adjust the position of the steel ball. The device has achieved good results in the experiment. Moon et al. [23] proposed an electromagnetic balance device based on the similar principle. He achieved the spindle balance experiment by means of the influence coefficient method at 14400 rpm. In 2008, Japan Nakamoto et al. [24] designed a new type of balance device that uses magnetic fluid as a balancing mass. By changing the magnetic field distribution in the periphery of the balance terminal, the purpose of changing the magnetic fluid distribution in the terminal was verified. The device was validated at 6,000 rpm. A new electromagnetic ring balancer for active imbalance compensation of rotating machinery was proposed by Fan et al. [25] in 2014. He verified the feasibility and effectiveness of balancing devices. Although they have studied different implementations, most of them use the ICM to verify the device. The ICM is a kind of test weight method. Test weight is needed to calculate the unbalance vector of the rotor system and then readjust the counterweight to achieve the purpose of correcting the vector. However, this method does not apply to weighted online balancing due to the test weight, such as spray online balancing. The no trial weight balance method can effectively solve the above problems. In addition, the spray dynamic balancing balance has high precision and can perform multiple online dynamic balancing, which is very suitable for high-precision loading.

The no trial weight spray online dynamic balancing technology is studied in this paper. This method can quickly identify unbalanced vectors and achieve high-precision loading. Therefore, it can achieve high-efficiency and high-precision online vibration suppression. An integrated balanced terminal (IBT) using 3D rapid prototyping technology was first proposed by our research group compared with the traditional spray online balancing technology. The IBT perfectly solved the problems of sealing and high-speed spin-off of traditional assembled balanced terminals. This technology is important for improving the accuracy of precision rotating machinery.

2. No Trial Weight Balance Method of Spindle

The influence coefficient method used in the industrial field is a kind of method that causes the response of the target

rotor system by adding trial weights. The aggravated influence coefficient matrix of the rotor system can be obtained. However, the influence coefficient matrix is not a virtual matrix. It is a characteristic parameter that can reflect the response of the rotor system when excited by energy. This shows that this matrix is an inherent characteristic of the system. In other words, the unbalance vector $[\alpha]$ can be calculated by identifying the characteristic matrix of the rotor system. We combine the high-speed electric spindle designed by our laboratory to study the WTWBM. The structure is shown in Figure 1.

This high-speed spindle system was developed specifically for studying online balancing. The maximum rotational speed of the spindle is 40,000 rpm. A pair of bearings SNFA VEX35 are mounted on the spindle and arranged in a back-to-back layout and preloaded by two sleeves and a locknut. The bearings are lubricated with oil mist, and the spindle is cooled by circulating water cooling. It should be noted that 1 : 7 taper is designed at the front and rear ends of the spindle to mount the counterweight disc.

It is necessary to establish the dynamic model of the spindle in order to identify the unbalance vector. The rotor system of spindle can be discretized into discs, elastic shaft sections, and bearing units. The rotor is divided into 50 nodes to form 49 units. The coordinate system is established with the rotor axis as the axis. The finite element model of the rotor system is shown in Figure 2.

The beam element has a simple structure and is easy to program, so it is still the first choice for establishing a finite element model. The Timoshenko beam element consisting of two nodes is shown in Figure 3. The motion of each node consists of five degrees of freedom, namely, three translational degrees of freedom $\delta_x, \delta_y, \delta_z$ and two rotational degrees of freedom γ_y, γ_z, where the X-axis torsional freedom is not considered [26, 27].

Regardless of the internal damping of the beam, the equation of motion of the beam can be expressed as follows [28]:

$$[M^b]\{\ddot{q}\} - \Omega[G^b]\{\dot{q}\} + ([K^b] + [K^b]_P - \Omega^2[M^b]_C)\{q\} = \{F^b\},$$

(1)

where $[M^b]$ is mass matrix, $[M^b]_C$ is additional mass matrix considering effect of centrifugal force, $[G^b]$ is symmetrical gyro matrix, $[K^b]$ is stiffness matrix, $[K^b]_P$ is additional stiffness matrix due to axial loading, $\{q\}$ is system displacement vector, and $\{q\} = \{\delta_x, \delta_y, \delta_z, \gamma_y, \gamma_z\}^T$, $\{F^b\}$ is external force vector. The superscript ^{b} stands for the beam unit and Ω is the speed.

Similarly, the equation for the motion of the disk unit is given by the following eqaution:

$$[M^d]\{\ddot{q}\} - \Omega[G^d]\{\dot{q}\} = \{F^d\},$$

(2)

where $[M^d]$ is mass matrix, $[G^d]$ is gyro matrix, the superscript ^{b} stands for the beam unit. Assuming that the unbalanced mass is m_D and the eccentricity is e, the unbalance force is as follows:
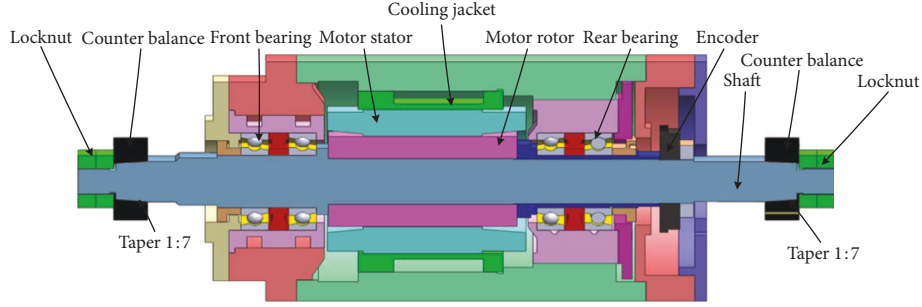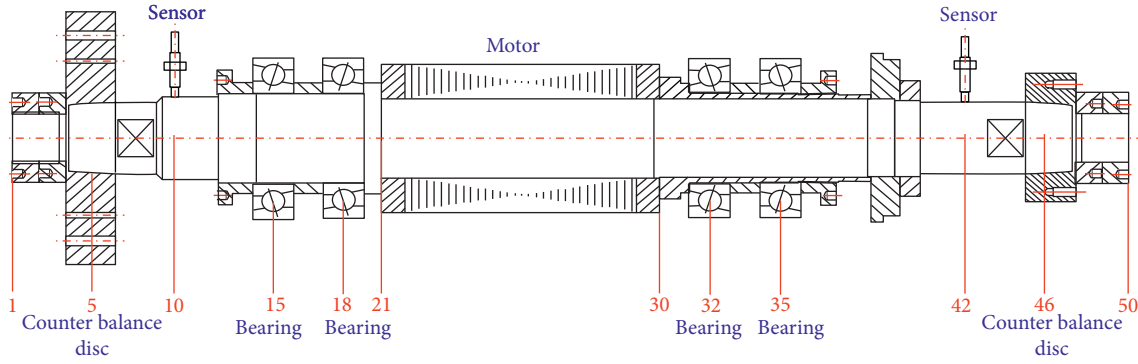
FIGURE 1: High-speed spindle model.

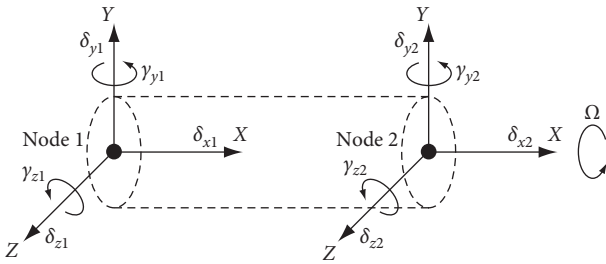FIGURE 2: Finite element model (node number: 1∼50).

FIGURE 3: Timoshenko beam element.

$$\{F^d\} = \left\{ \begin{array}{c} 0 \\ m_D e \Omega^2 \cos \Omega t \\ m_D e \Omega^2 \sin \Omega t \\ 0 \\ 0 \end{array} \right\},$$

$$\{q\} = \left\{ \begin{array}{c} u \\ v \\ w \\ \theta_y \\ \theta_z \end{array} \right\}.$$

(3)

In addition, the generalized forces acting on the bearings can be written as follows [29]

$$[C^c]\{q\} + [K^c]\{q\} = \{Q^c\}, \qquad (4)$$

where $[C^c]$ is the bearing damping matrix, $[K^c]$ is the bearing stiffness matrix, and $\{Q^c\}$ is the vector of generalized forces of the bearings.

In combination with the above derivation, the model of the spindle rotor, disc, and bears is integrated. The differential equation of the spindle system is as follows [30]:

$$[M]\{\ddot{x}\} + [C]\{\dot{x}\} + [K]\{x\} = \{F\}, \qquad (5)$$

where system mass matrix is $[M] = [M^b] + [M^d]$ and $[C]$ is system damping matrix, which can be obtained by modal analysis. The excitation F is due only to harmonic unbalance excitations $\{F^d\}$ under steady-state condition. The unbalance excitation force $\{F^d\}$ can be expressed as follows:

$$F^d = u \cdot e^{j\omega \cdot t}. \qquad (6)$$

Vibration response x is

$$x = r \cdot e^{[j(\omega \cdot t + \varphi)]}, \qquad (7)$$

where r is unbalanced response, u is unbalanced mass, and φ is lag angle. Substituting Eqs. (6) and (7) into Eq. (5) results in

$$\left\{ [K] - \omega^2 [M] + i\{[C] + [G]\}\omega \right\} \cdot r \cdot \exp(j\varphi) = u. \qquad (8)$$

The above formula can be written as $[\alpha] \cdot r = u$, where $[\alpha]$ is a aggravated influence coefficient matrix of the rotor system, which can be derived from the above equation:

$$[\alpha] = \left\{ [K] - \omega^2 [M] + i\{[C] + [G]\}\omega \right\}^{-1} \cdot \exp(-j\varphi). \qquad (9)$$
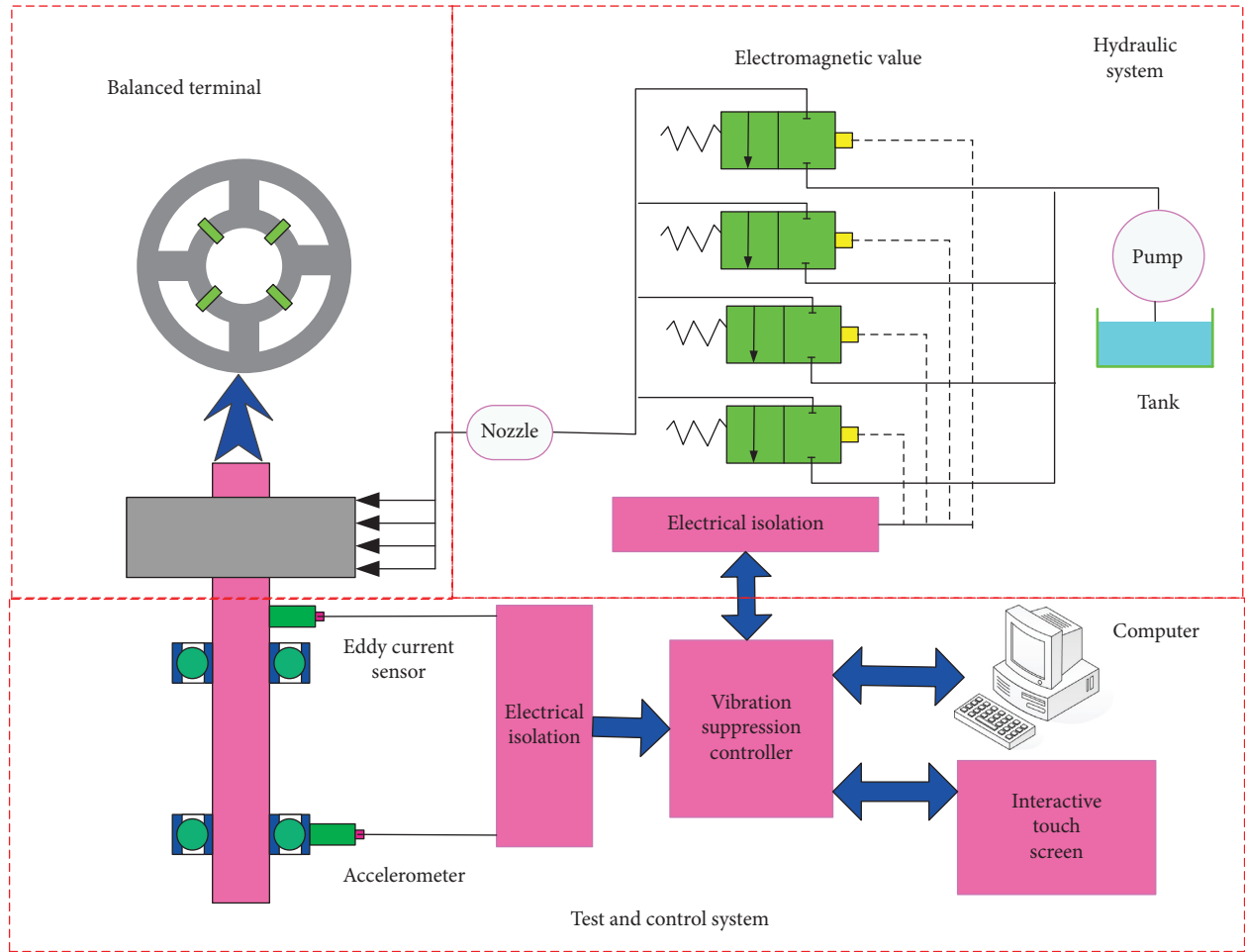
FIGURE 4: Spray online balance system structure.

From the above equation, it can be seen that the aggravated influence coefficient of the rotor system is determined by the mass, stiffness, lag angle, and rotation speed. That is to say, the aggravated influence coefficient of the rotor system is determined by the rotor structure parameters. It is an inherent parameter to reflect the energy transfer characteristics of the rotor system.

$$[Q] = -[\alpha]^{-1} \cdot A, \tag{10}$$

where $[Q]$ is balance vector, A is unbalanced vibration response obtained through testing, and the negative sign indicates that the phase difference between the balance vector and the imbalance is 180°. After calculating the balance vector, we apply it to the online dynamic balance by modifying the matching process, and the online weighted correction scheme can be obtained by rapid orientation iteration matching. The detailed online balance process is described later.

3. Online Balancing Experiment System

3.1. System Structure. The spray dynamic balance system developed by our research group was used to perform experimental research on the no trial weight online balance method. The structure of the spray online balancing system is shown in Figure 4. The system is mainly composed of balanced terminals, hydraulic systems, and measurement and control systems. The balance terminal is the key component of the dynamic balancing system, and its function is to store the correction mass. The main function of the hydraulic system is the quantitative delivery of liquid. The function of the measurement and control system is unbalanced vector calculation and hydraulic system control.

3.2. New Integrated Balance Terminal. Balancing terminals are the core components of spray dynamic balancing. The main function is to store the correction mass. Through investigation, it has been found that the balance terminal in the world is the assembled balanced terminal shown in Figure 5.

As can be seen from Figure 5, the traditional assembled balance terminal is assembled from the inner ring and from the outer ring through interference fit. However, the deformation of the outer ring of the balanced terminal is larger than that of the inner ring under the action of centrifugal force. When the balanced terminal rotates with the spindle at a high speed, the magnitude of interference between the inner and outer rings of the balanced terminal will decrease. This will lead to a drop in the sealing performance of the balanced terminal or even complete failure. According to the theory of
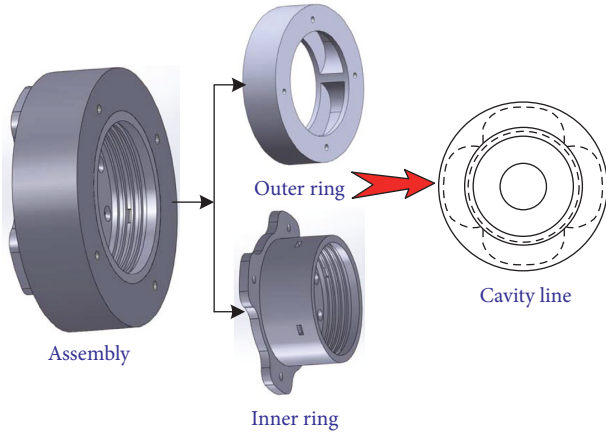
FIGURE 5: Assembled balanced terminal schematic.

FIGURE 6: Relationship between radial displacement and speed.

elasticity [31], regardless of the tangential displacement component of the inner and outer rings in the rotation process, the radial centrifugal force of the inner and outer rings is applied as a unit volume force, which can be equivalent to the problem of axisymmetric plane stress. At any radius r, the deformation displacement u_r is [32]

$$u_r = \frac{3+\nu}{8E}\rho\omega^2 r\left[(1-\nu)\left(B^2 + A^2\right) + (1+\nu)\frac{A^2 B^2}{r^2} - \frac{1-\nu^2}{3+\nu}r^2\right],$$
(11)

where ω is angular velocity; ρ is material density; E is elastic modulus; ν is Poisson's ratio; and A and B are the diameters of the inner and outer rings, respectively. Then, the minimum allowable amount of interference δ is shown as follows:

$$\delta = u_o\left(R_F\right) - u_i\left(R_F\right) = \frac{3+\nu}{4E}\rho\omega^2 R_F\left(R_O^2 - R_I^2\right),$$
(12)

where R_F is the critical radius of the inner and outer rings ($R_F = 33$ mm), R_O is the outer radius of the outer ring of the dynamic balance terminal ($R_O = 47$ mm), and R_I is inner radius of the inner ring of the balancing terminal ($R_I = 28$ mm). Balanced terminal material is titanium alloy (). When the magnitude of interference is $20\,\mu$m, the relationship between the radial expansion of the inner and outer rings and the rotation speed is shown in Figure 6. It can be seen that when the rotational speed reaches the loose critical speed, the interference connection will fail. So, the assembled balance terminal not only loses the capacity of the chamber seal but also has potential safety hazards. Of course, the magnitude of interference cannot be too large. If the magnitude of interference is too large, assembly will be difficult. Pressing in force will even cause fatigue damage to the inner and outer rings.

Because of the above problems in the traditional assembly balanced terminals, an integrated balanced terminal that combines the needs of spray online dynamic balancing and the technical features of rapid prototyping was proposed
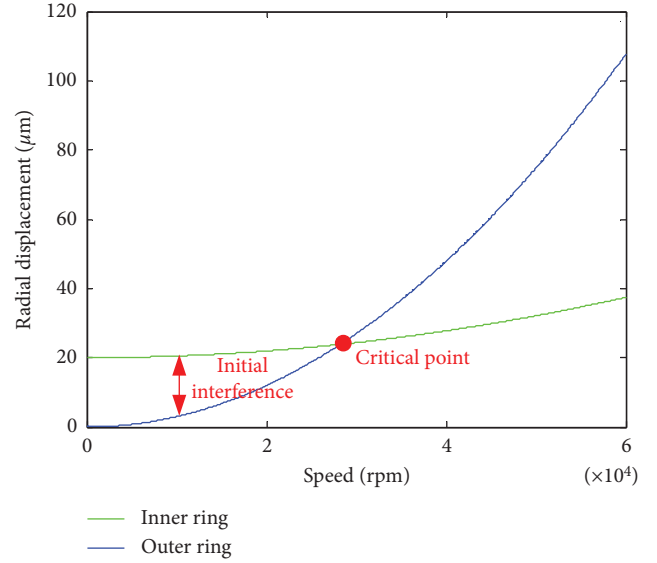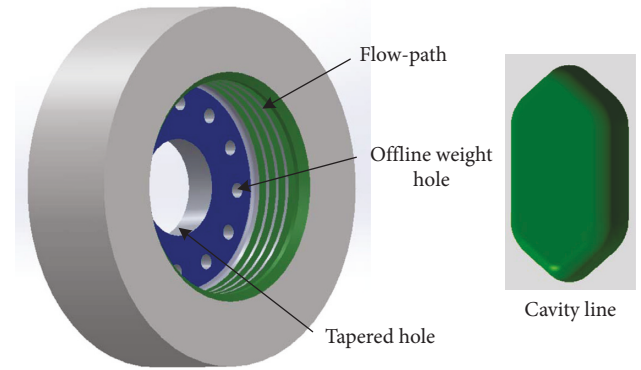

FIGURE 7: Integrated balance terminal diagram.

by our research group as shown in Figure 7. The integrated balancing terminal eliminates the traditional design of the inner and outer rings. It is mainly composed of the terminal body, flow path, offline weight holes, tapered holes, and chambers. The integrated balanced terminal is formed in one time using 3D printing technology. The tapered holes are used to connect with the spindle. The function of offline weight holes is to eliminate the initial eccentricity of the balanced terminal in the manufacturing process. This will not cause new additional imbalance to the spindle. The function of the flow path is to direct the fluid to the corresponding chamber.

The capacity of the integrated balanced terminal determines its balance capacity. In order to calculate the balance capacity of the balanced terminal, the volume of chamber must be calculated. In order to simplify the calculation, the corner is ignored and the cross section shown in Figure 8(a) is obtained; the integral microelement is shown in Figure 8(c).
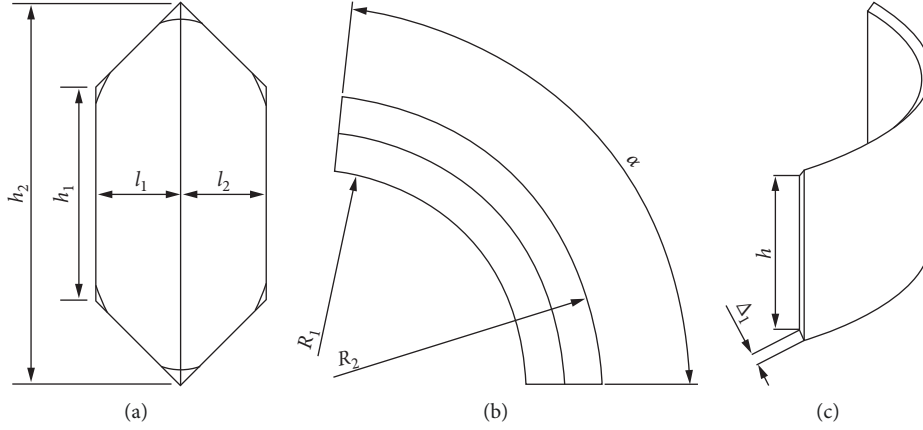
FIGURE 8: Calculation model. (a) Section. (b) Top view. (c) Microelement.

Then, the volume of a single liquid chamber is given by

$$V_1 = \frac{2\pi\alpha}{360} \int_0^{l_1} (R_1 + l)(h_1 + 2l)dl,$$

$$V_2 = \frac{2\pi\alpha}{360} \int_0^{l_2} (R_1 + l_1 + l)(h_2 - 2l)dl, \quad (13)$$

$$V = V_1 + V_2,$$

where $h_1 = 14.5$ mm, $h_2 = 26$ mm, $l_1 = l_2 = 5.75$ mm, $R_1 = 33$ mm so, $V \approx 13230$ mm^3

Assume that the density of the weighted liquid is ρ, the maximum balance capacity of a single liquid chamber:

$$Q_1 = \frac{2\pi\rho\alpha}{360} \int_0^{l_1} (R_1 + l)(h_1 + 2l)(33 + l)dl,$$

$$Q_2 = \frac{2\pi\rho\alpha}{360} \int_0^{l_2} (R_1 + l_1 + l)(h_2 - 2l)(33 + l_1 + l)dl, \quad (14)$$

$$Q = Q_1 + Q_2,$$

where $\rho = 0.8$ g/mm^3, so, $Q \approx 413$ g·mm. It can be known from the balanced terminal cavity distribution structure that when the adjacent two chambers are filled with the balance liquid and the other chambers are all empty, the balancing capacity of the balanced terminal will reach the maximum value at this time. The maximum is $\sqrt{2}Q = 584$ g·mm.

The balancing terminal rotates with the spindle at a high speed. So, balancing the liquid in the terminal chamber will stress the chamber due to centrifugal force. Assuming the rotational speed is 30000 rpm, the cavity of the balance terminal is filled with the weight fluid with density 0.8 g/mm^3, and the centrifugal force produced by the weight fluid in a single cavity can be calculated by the following equation:

$$F = m\omega^2 r = Q\omega^2, \quad (15)$$

where m is the liquid mass in the cavity, r is the radial distance between the center of gravity of the counterweight

fluid and the axis of rotation, ω is the angular velocity, and $Q = m \times r$; hence, centrifugal force $F = 4096$ N.

When the balanced terminal rotates at a high speed, most of the water pressure generated by the centrifugal force will act on the outer surface of the cavity, and the outer surface of the cavity is not a regular plane. To simplify the calculation, the pressure area on the outer surface of the chamber is equivalent to the projection surface as shown in Figure 9. When the balanced terminal is filled with the counterweight fluid, the pressure on the outer surface of the chamber is calculated by the following equation:

$$P = \frac{F}{S} = \frac{F}{(2\alpha/360)(\pi R_2 h_2)}, \quad (16)$$

where centrifugal force $F = 4076$ N, $\alpha = 84°$, radius $R_2 = 44.5$ mm, and thickness $h_2 = 26$ mm; thus, the pressure $P = 2.4$ MPa.

In order to select the thickness of the cavity wall of the balanced terminal, the analysis was carried out under the extreme conditions (full-chamber liquid and 30,000 rpm). When the pressure is 2.4 MPa, different thicknesses of the cavity arc surface force analysis model are built in ANSYS as shown in Figure 10.

The relationship between the material thickness and the stress and deformation of the titanium alloy balance terminal surface is shown in Figure 11. It can be seen that when the material thickness is selected as 2 mm under the extreme conditions, the stress value and deformation tend to be stable. Therefore, in order to meet the requirement of the balanced terminal with the spindle acceleration and deceleration, the wall thickness of the force surface should be greater than 2 mm. We have designed the thickness of the balanced terminal force surface to be 2.5 mm.

The assembled balance terminal of different materials was trial-produced by us as shown in Figure 12. By analyzing the requirements of 3D printing technology and strength, titanium alloy is selected as the manufacturing material for the integrated balance terminal.

So, the integrated balanced terminal manufactured according to the design parameters is shown in Figure 13(a). For the nonblocking of the liquid flow and balancing the
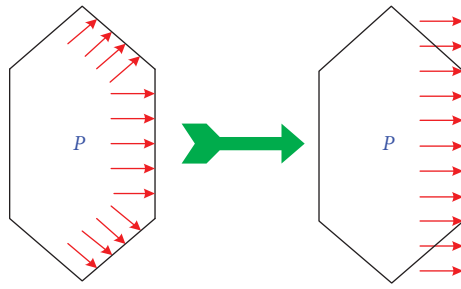
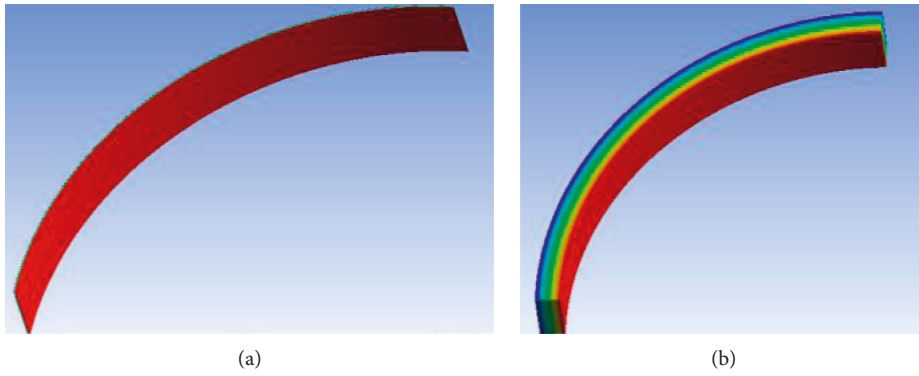FIGURE 9: Fluid pressure on the cavity surface.

(a)   (b)
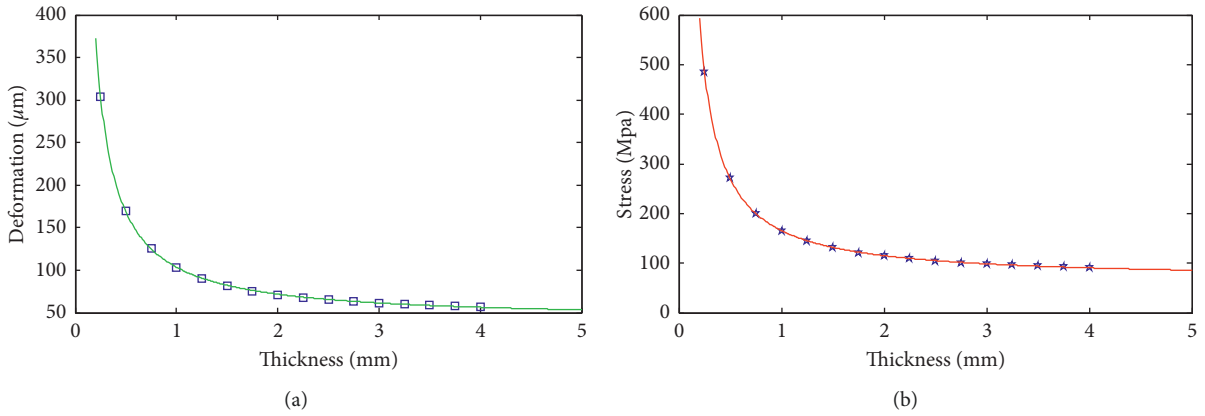
FIGURE 10: Surface force analysis model.

(a)   (b)

FIGURE 11: The relationship between thickness and stress and deformation.

(a)   (b)   (c)

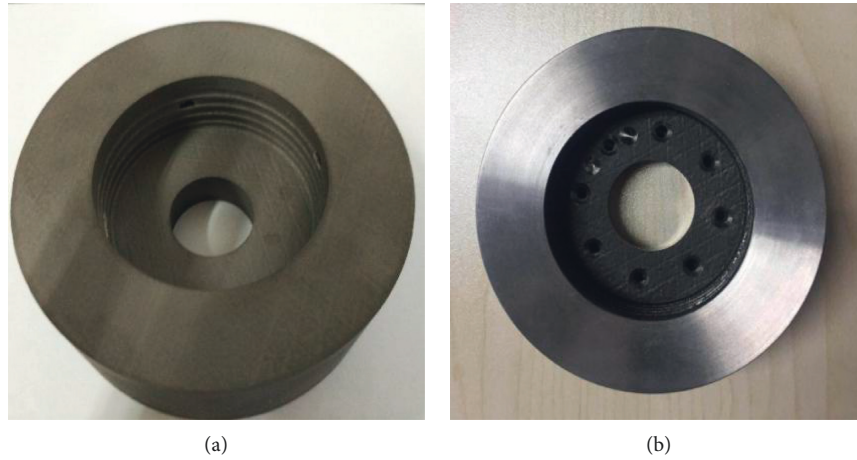FIGURE 12: Assembled balance terminal. (a) Steel-45#. (b) Aluminum alloy-7A04. (c) Titanium alloy-TC4.

(a)

(b)

FIGURE 13: Titanium alloy integrated balancing terminal. (a) Before modification. (b) After modification.
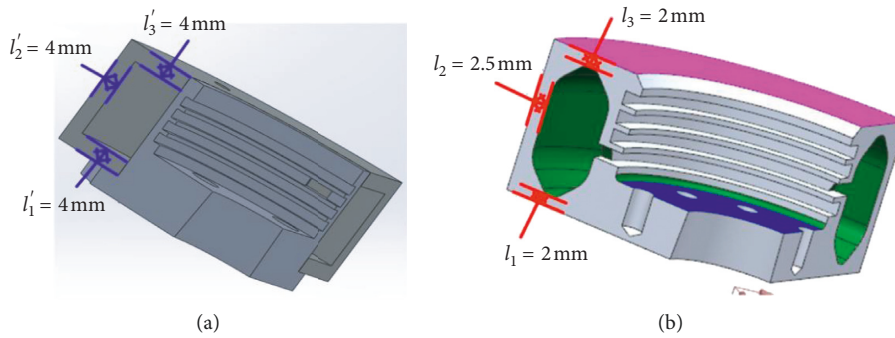

(a)

(b)

FIGURE 14: Comparison of 1/4 model. (a) Assembled terminal. (b) Integrated terminal.

TABLE 1: Comparison of two balanced terminal parameters.

Species	Parameters				
	Balance ability (g·mm)	Thickness (mm)	Volume (mm^3)	Mass (g)	Price (RMB)
Assembled terminal	489	38	160549	562	10240.00
Integrated terminal	584	28	83780	387	5804.00
Variation (%)	⬆19.4	⬇26.3	⬇47.8	⬇31.1	⬇43.3

signal test on the terminal surface, the flow channel and the surface were modified as shown in Figure 13(b). The balancing terminal is balanced to eliminate the initial mass eccentricity on the balancing machine. This will not cause new additional imbalance to the spindle.

The 1/4 model of assembled balanced terminals and integrated balanced terminals is shown in Figure 14. The parameters of the two balanced terminals are shown in Table 1. It can be seen that the integrated balanced terminal designed in this paper has obvious advantages in comparison with the assembled balanced terminal. The maximum balance capacity of balanced terminal increased from 489 g·mm to 584 g·mm. On the basis of a 19.4% increase in balance capacity, thickness dropped from 38 mm to 28 mm, a drop of 26.3%. The volume of balanced terminal dropped from 160549 mm^3 to 83780 mm^3 with 47.8% drop ratio. The mass of balanced terminal has dropped from 562 g to 387 g with

a drop ratio of 31.1%, so that the additional mass added by the balanced terminal to the spindle will be effectively reduced.

3.3. Balanced Procedure and Software. The no trial weight balance method is applied to the spray online balance system, which can achieve efficient online balance, thus maximizing the protection automation processing link. The flow diagram of the no trial weight spray online dynamic is shown in Figure 15, in which three main steps are included: (1) acquisition process of rotor structural parameters; (2) acquisition process of counterweight scheme; and (3) online balance process. The balancing procedure is as follows:

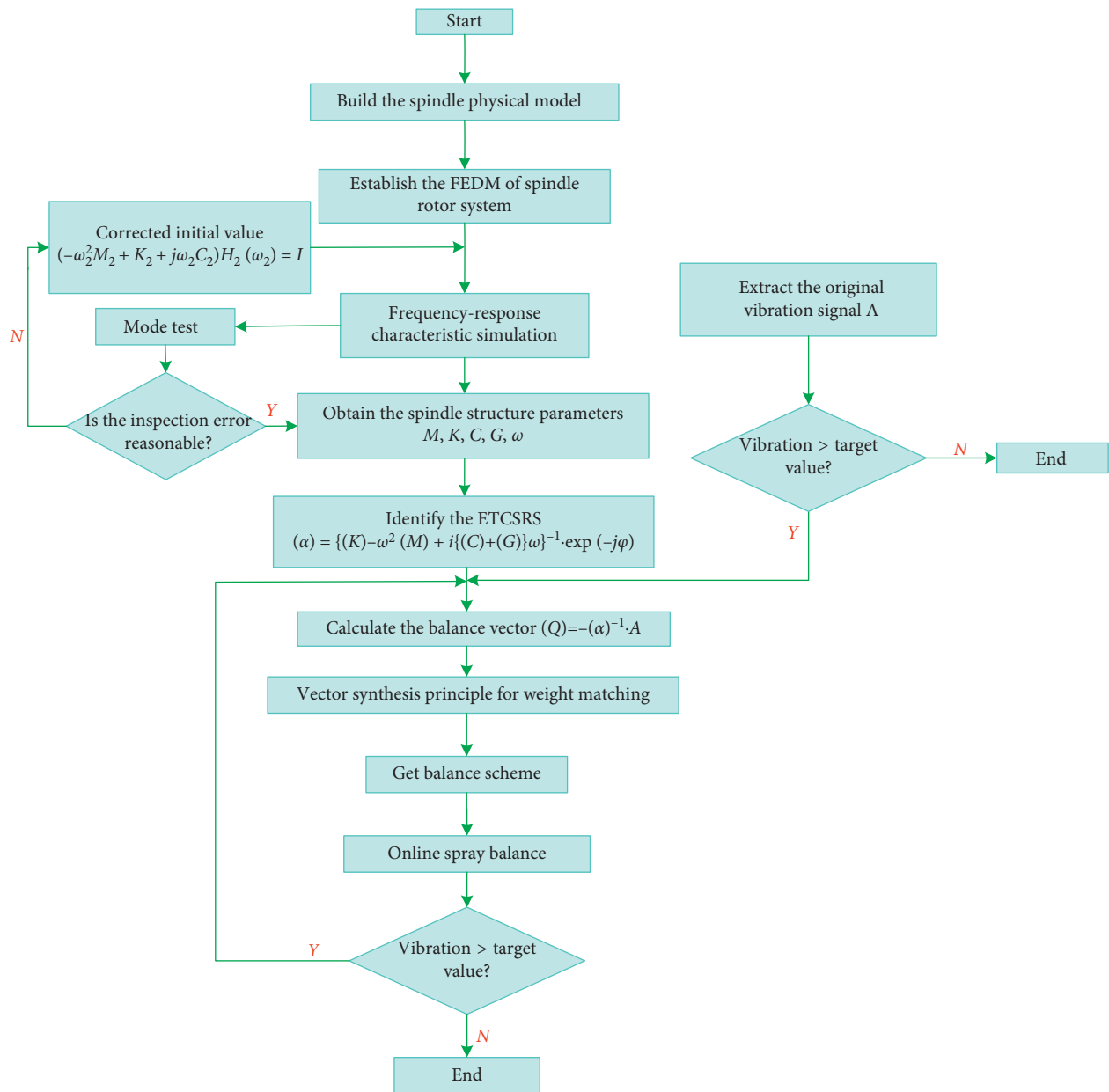(1) Establish the physical model and finite element model of the spindle rotor system by separating the rotor model

FIGURE 15: The balance procedure.

(2) Obtain the structural parameters of the spindle rotor system, such as mass matrix M, stiffness matrix K, and damping matrix C by the finite element simulation and simulate the inherent modal characteristics of the spindle

(3) Substitute the correction matrices of structural parameters in Equation (9) to identify the aggravated influence coefficient matrix

(4) Extract the original vibration signal of the spindle and the phase information corresponding to the vibration signal; substitute aggravated influence coefficient matrix into Equation (10) to calculate the unbalance vector

(5) The weighting scheme is searched according to the cavity angle and the unbalance vector

(6) The spray online dynamic balancing system is injected into the corresponding cavity to correct the unbalance vector.

According to the balance flow chart, a measurement and control system based on virtual instruments was developed by our research group. The operation interface is shown in Figure 16. The no trial weight online balance measurement and control software consists of vibration signal monitoring, trend of vibration displacement change, vibration status display and monitoring, liquid state display and monitoring, and online balance information records.
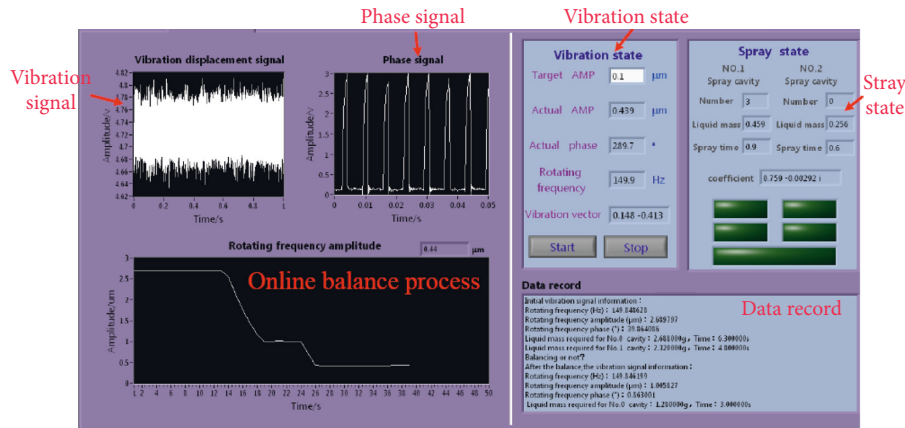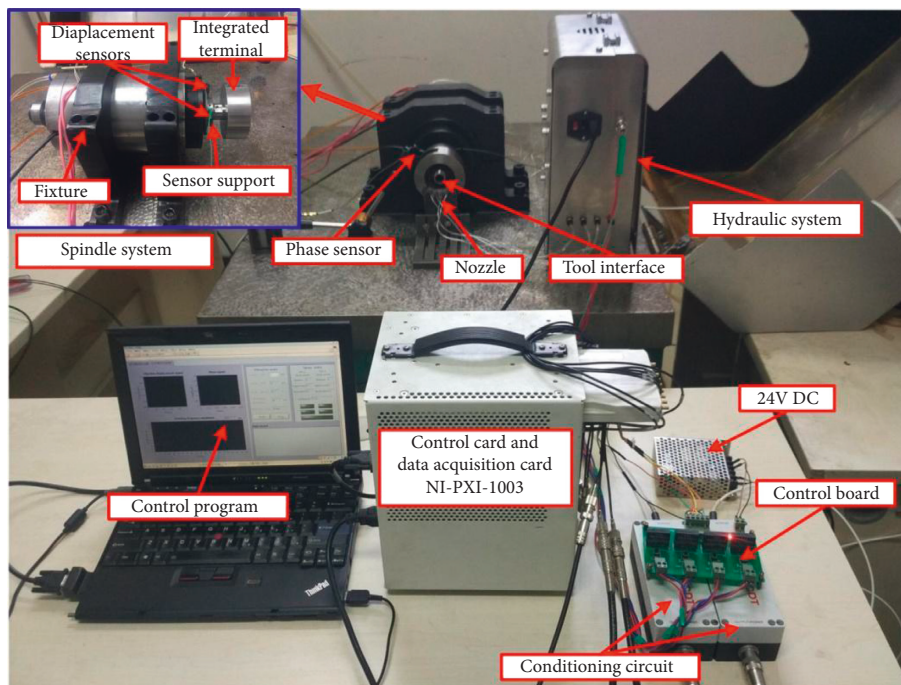
Figure 16: Measurement and control panel.

Figure 17: Experimental setup.

4. Methods and System Validation

4.1. Experimental Setup. In order to verify the application of no trial weight spray online dynamic on high-speed spindle, the high-speed spindle comprehensive performance test bed was designed by our research group as shown in Figure 17. The test bed comprises a spindle 150 SD40Q7 (Figure 1) whose maximum rotational speed is 40,000 rpm, and two pairs of SNFA VEX35 bearings lubricated by oil mist are mounted on the spindle with a clearance tolerance to avoid the preload variation. The water cooling system controls the temperature variation. The balancing discs are installed on the ends of the spindle to suppress vibration. A rotating encoder mounted on the shaft feedbacks the rotational speed. The spindle rotor is designed with a ratio of $1:7$ tapered to install the integrated balancing terminal, and the

balancing terminal is fixed with a locknut. In the front of the rotor, a HSK C32 tool holder interface is designed. The measuring equipment is composed of a synchronous acquisition system developed by our research group. A National Instrument PXI-4472 was used to extract vibration and phase information. German Micro-Epsilon U-05 eddy-current sensor (range 0.5 mm; resolution 0.025 μm) is used to measure vibration displacement. The NI-PXI6123 is used to control the hydraulic system. A photoelectric sensor was applied to measure the phase. The layout of the experimental setup is shown in Figure 18.

4.2. Measurement Principles. The system carries out real-time synchronous acquisition of vibration using eddy-current displacement sensors mounted along the X-axis
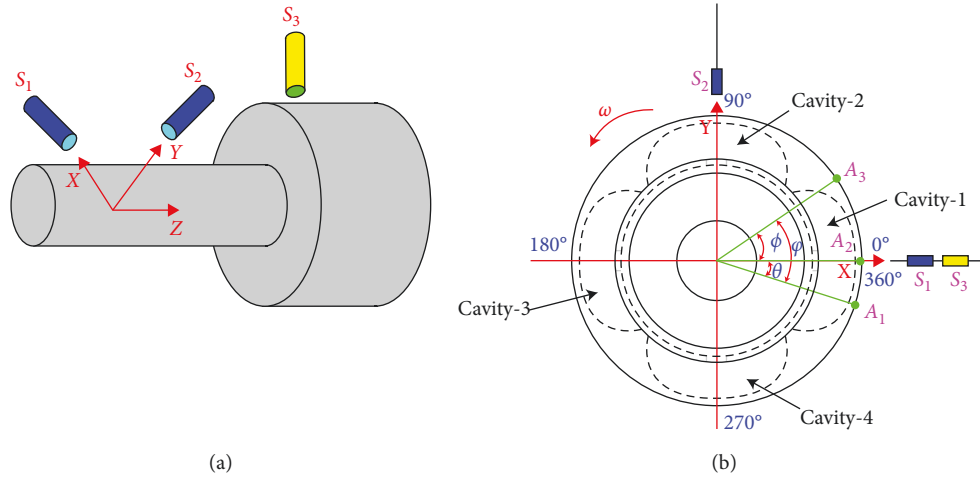
(a)

(b)

FIGURE 18: Measurement principles. (a) Sensor layout. (b) Angle relation.
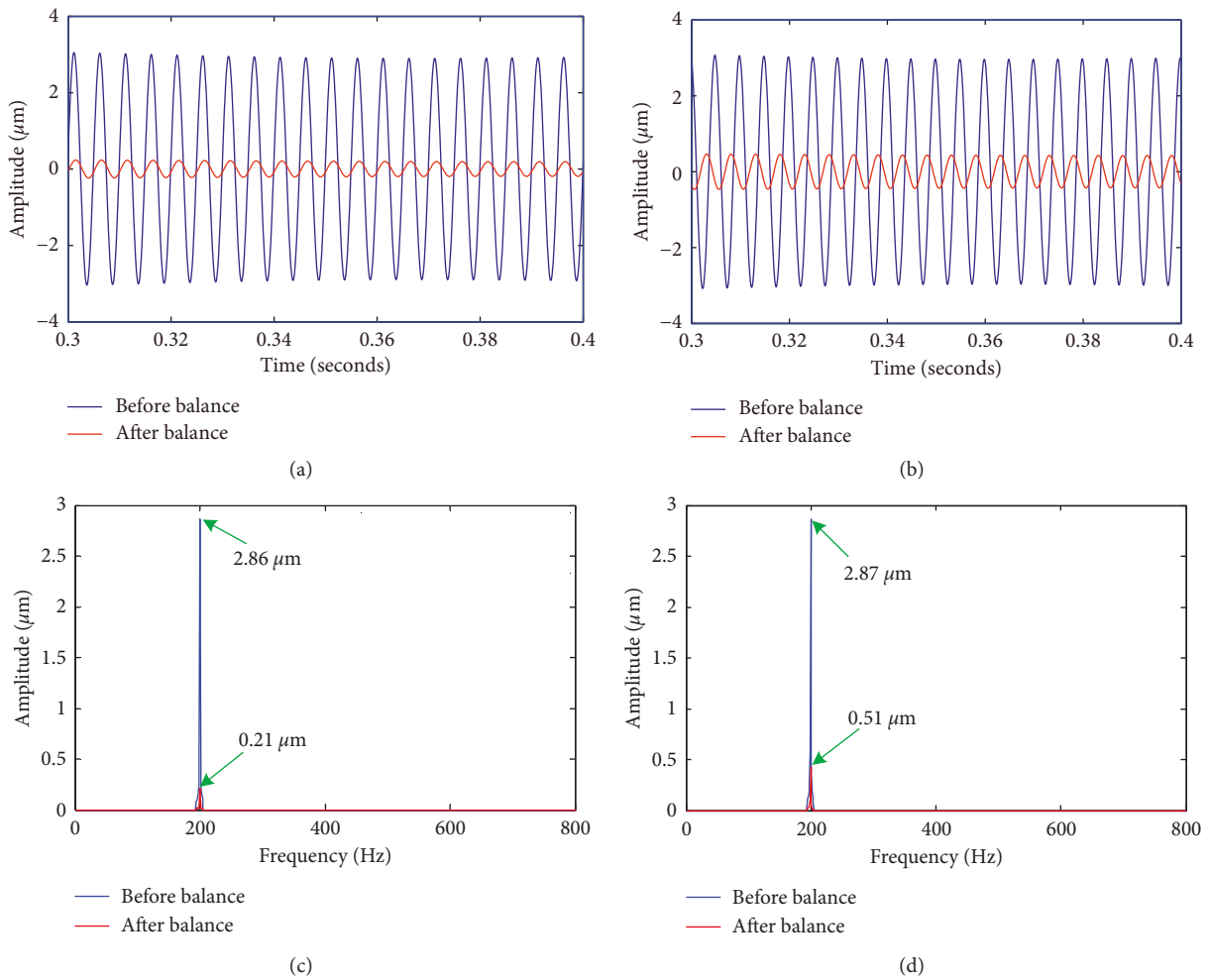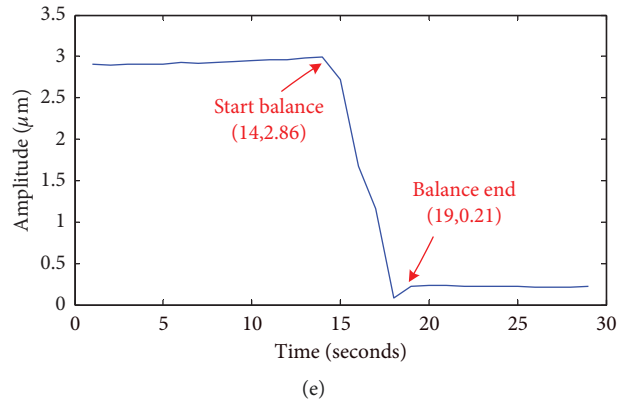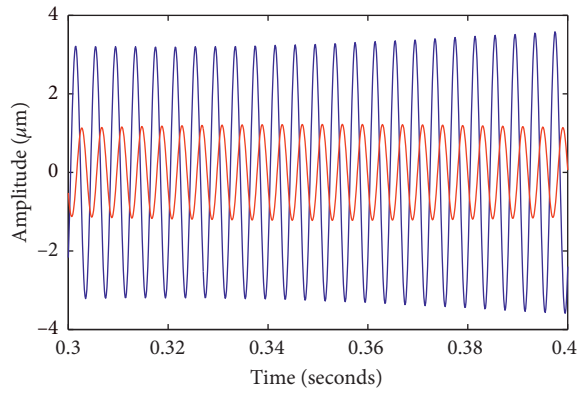

(a)

(b)

(c)

(d)

FIGURE 19: Continued.

(e)

FIGURE 19: Comparison of balance information in the *X*-*Y* direction at 12,000 rpm. (a) *X*-time domain. (b) *Y*-time domain. (c) *X*-frequency domain. (d) *Y*-frequency domain. (e) Online balance process.

(a)

(b)

(c)
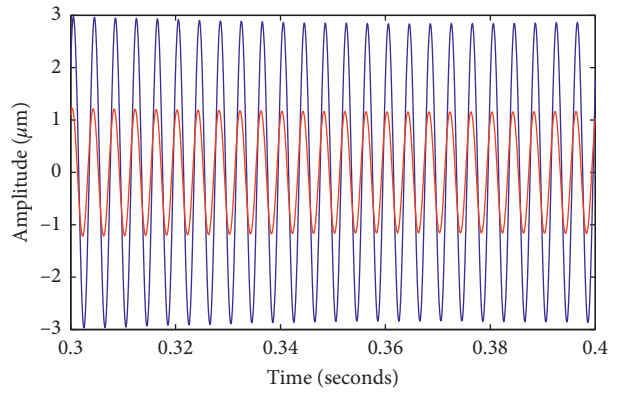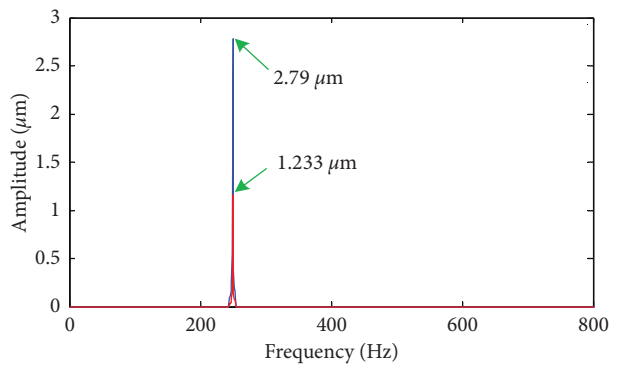

(d)

FIGURE 20: Continued.

(e)

FIGURE 20: Comparison of balance information in the *X*-*Y* direction at 15,000 rpm. (a) *X*-time domain. (b) *Y*-time domain. (c) *X*-frequency domain. (d) *Y*-frequency domain. (e) Online balance process.

FIGURE 21: Continued.

(e)

FIGURE 21: Comparison of balance information in the *X-Y* direction at 18,000 rpm. (a) *X*-time domain. (b) *Y*-time domain. (c) *X*-frequency domain. (d) *Y*-frequency domain. (e) Online balance process.
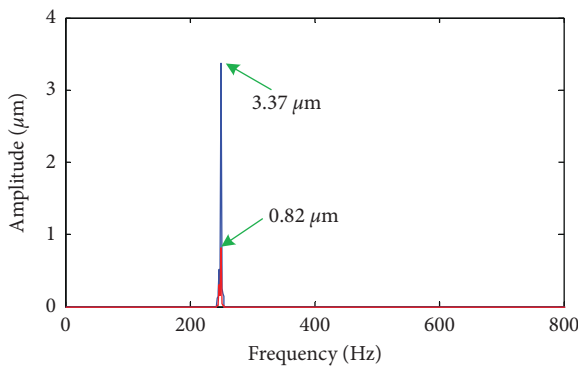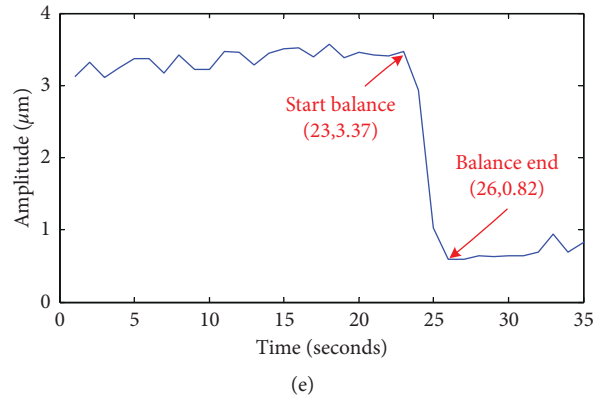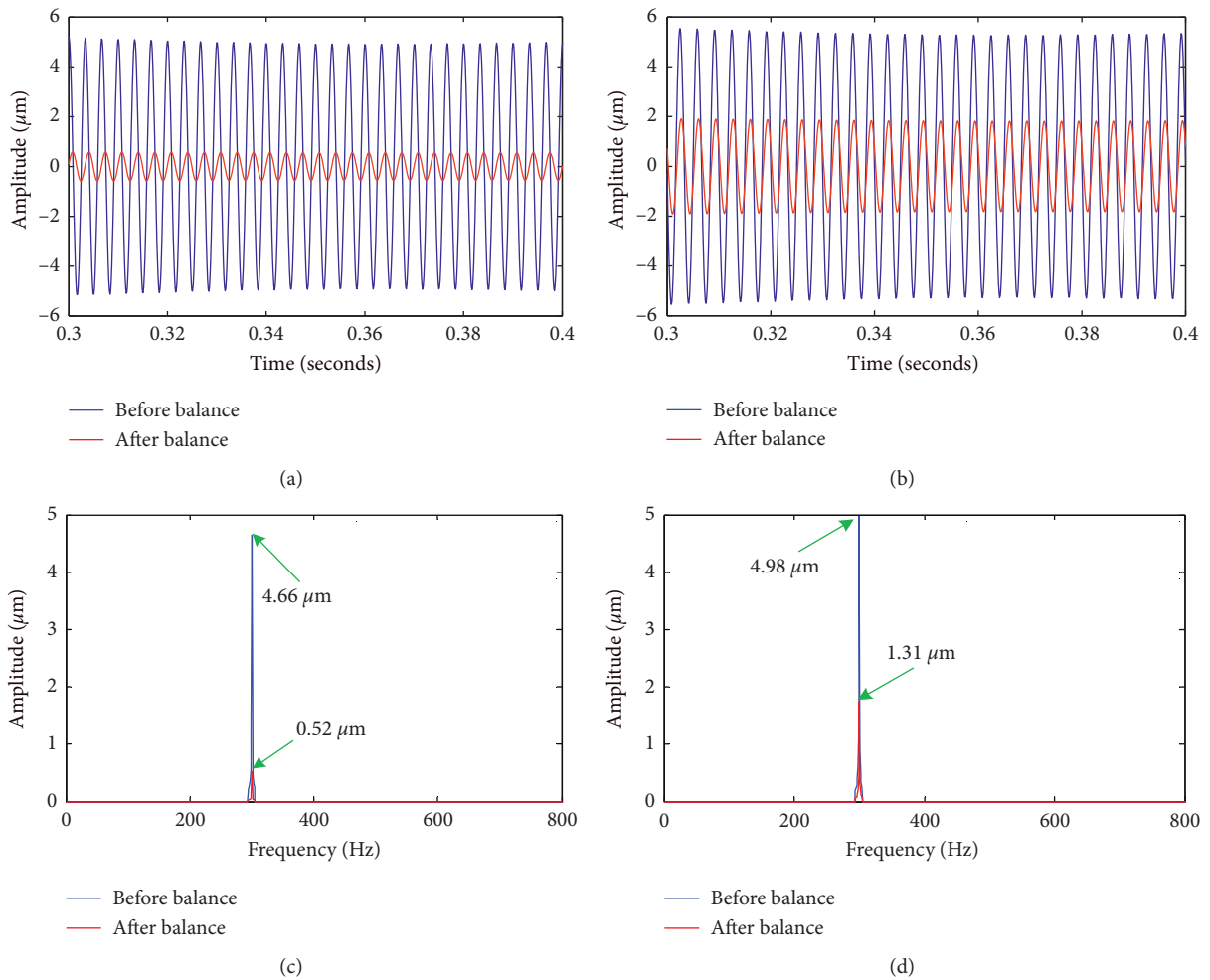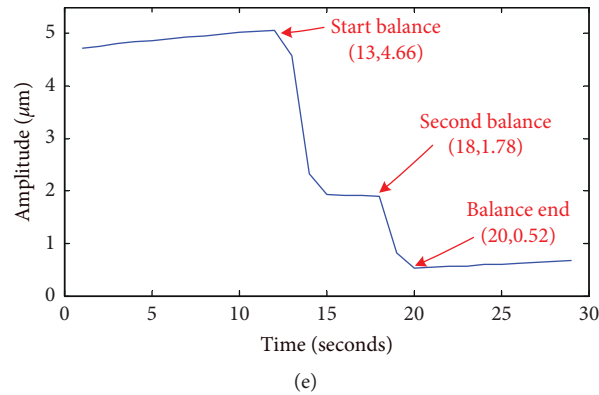
(S_1) and the *Y*-axis (S_2); the layout is shown in Figure 18(a). The photoelectric sensor (S_3) mounted on the *X*-axis measured the phase (Figure 18(b)). The *X*-direction displacement sensor S_1 and the phase sensor S_3 are aligned with the zero-hole position to simplify the complex angular relationship and eliminate the influence of the initial phase angle. Then, the lag angle (φ) can be obtained from Equation (17). In Figure 18(b), A_1 is vibration peak point, A_2 is phase point, and A_3 is equivalent point of the rotor unbalance force.

$$\varphi = \theta + \phi. \tag{17}$$

4.3. Experimental Results Analysis. The pressure of the hydraulic system in the experiment is 0.12 MPa and spraying unit time is 100 ms. The *X*-direction vibration displacement is used as the balance reference. In order to accurately extract the imbalance characteristics, harmonic wavelet technology was used to extract the frequency characteristics [33]. The online balance experiments at multiple speeds were verified in the experimental system as shown in Figure 17.

Comparison of rotation frequency amplitude before and after balancing at 12,000 rpm, 15,000 rpm, and 18,000 rpm is shown in Figures 19–21. It can be seen from Figure 19 that the vibration amplitude in the *X* direction decreases from 2.86 μm to 0.21 μm, the drop ratio reaches 92.66%, and the vibration amplitude in the *Y* direction decreases from 2.87 μm to 0.51 μm with 82.23% drop ratio at 12,000 rpm. It can be seen from the online balance process that the spray weight is only needed once, and the total online balancing time is 5 seconds.

It can be seen from Figure 20 that the vibration amplitude in the *X* direction decreases from 3.37 μm to 0.82 μm, the drop ratio reaches 75.67% and the vibration amplitude in the *Y* direction decreases from 2.79 μm to 1.23 μm with 55.91% drop ratio at 15,000 rpm. It can be seen from the online balance process that the spray weight is only needed once and the total online balancing time is 3 seconds.

It can be seen from Figure 21 that the vibration amplitude in the *X* direction decreases from 4.66 μm to 0.52 μm, the drop ratio reaches 88.84%, and the vibration amplitude in the *Y* direction decreases from 4.98 μm to 1.31 μm with

73.69% drop ratio at 18,000 rpm. It can be seen from the online balance process that the spray weight is two times and the total online balancing time is 7 seconds.

5. Conclusions and Further Work

A no trial weight spray online balance method is proposed. A high-speed spindle finite element analysis model was established, and the dynamic influence coefficient matrix was identified. A no trial weight spray online dynamic balancing system was developed, which has the advantages of no trial weight and high-precision loading. A new type of integrated balancing terminal that was formed using 3D printing technology was first proposed by our research group, and its advantages in various aspects are significantly higher than traditional assembly balanced terminals. Online balance experiments demonstrate the effectiveness of balancing methods and integrated balancing terminals.

It is important to note that the shaft is rigid. And, the focus is on one end of the bearing which is treated as a single-plane balancing problem. But the proposed method in this paper can be extended to both planes. We will further develop in-depth research on the method of no trial weight online dynamic balance considering dynamic stiffness, and we will further improve the loading accuracy of online balance system.

Data Availability

The data used to support the findings of this study are available from the corresponding author upon request.

Conflicts of Interest

The authors declare that there are no conflicts of interest regarding the publication of this article.

Acknowledgments

References

[1] S. Zhang and Z. Zhang, "Research on the field dynamic balance technologies for large diesel engine crankshaft system," *Shock and Vibration*, vol. 2017, Article ID 7150472, 10 pages, 2017.

[2] Y. Zhang, X. Mei, M. Shao, and M. Xu, "An improved holospectrum-based balancing method for rotor systems with anisotropic stiffness," in *Proceedings of Institution of Mechanical Engineers, Part C: Journal of Mechanical Engineering Science*, vol. 227, no. 2, pp. 246–260, 2013.

[3] X. Qiao and G. Hu, "Active control for multinode unbalanced vibration of flexible spindle rotor system with active magnetic bearing," *Shock and Vibration*, vol. 2017, Article ID 9706493, 9 pages, 2017.

[4] C. Yue, X. Ren, Y. Yang, and W. Deng, "Unbalance identification of speed-variant rotary machinery without phase angle measurement," *Shock and Vibration*, vol. 2015, Article ID 934231, 11 pages, 2015.

[5] H. Cao, X. Zhang, and X. Chen, "The concept and progress of intelligent spindles: a review," *International Journal of Machine Tools and Manufacture*, vol. 112, pp. 21–52, 2016.

[6] P. Xin, W. Hai-Qi, G. Jin-Ji, and M. Yu-Zhe, "Study on online active balancing system of rotating machinery and target control method," *WSEAS Transaction on Systems*, vol. 13, 2014.

[7] P. Gnielka, "Modal balancing of flexible rotors without test runs: an experimental investigation," *Journal of Sound and Vibration*, vol. 90, no. 2, pp. 157–172, 1983.

[8] Y. Kang, Y. P. Chang, M.-H. Tseng, P.-H. Tang, and Y.-F. Chang, "A modified approach based on influence coefficient method for balancing crank-shafts," *Journal of Sound and Vibration*, vol. 234, no. 2, pp. 277–296, 2000.

[9] M. B. Deepthikumar, A. S. Sekhar, and M. R. Srikanthan, "Modal balancing of flexible rotors with bow and distributed unbalance," *Journal of Sound and Vibration*, vol. 332, no. 24, pp. 6216–6233, 2013.

[10] L. S. Qu, H. Qiu, and G. H. Xu, "Rotor balancing based on holospectrum analysis: principle and practice," *Chinese Journal of Mechanical Engineering*, vol. 9, no. 1, pp. 60–63, 1998.

[11] G. Bin, X. Li, Y. Shen, and W. Wang, "Development of whole-machine high speed balance approach for turbomachinery shaft system with N + 1 supports," *Measurement*, vol. 122, pp. 368–379, 2018.

[12] R. S. Srinivas, R. Tiwari, and C. Kannababu, "Application of active magnetic bearings in flexible rotordynamic systems—a state-of-the-art review," *Mechanical Systems and Signal Processing*, vol. 106, pp. 537–572, 2018.

[13] E. P. Delgado and R. H. Bannister, "Balancing of an experimental rotor without trial runs," *International Journal of Rotating Machinery*, vol. 8, no. 2, pp. 99–108, 2007.

[14] S. Liu and L. Qu, *A New Field Balancing Method of Rotor Systems Based on Holospectrum and Genetic Algorithm*, Elsevier Science Publishers B. V, New York, NY, USA, 2008.

[15] L. Qu, X. Liu, G. Peyronne, and Y. Chen, "The holospectrum: a new method for rotor surveillance and diagnosis," *Mechanical Systems and Signal Processing*, vol. 3, no. 3, pp. 255–267, 1989.

[16] S. Liu, "A modified low-speed balancing method for flexible rotors based on holospectrum," *Mechanical Systems and Signal Processing*, vol. 21, no. 1, pp. 348–364, 2007.

[17] J. Niebsch and R. Ramlau, "Mathematical imbalance determination from vibrational measurements and industrial applications," in *Progress in Industrial Mathematics at ECMI*, pp. 293–298, Springer, Berlin, Germany, 2008.

[18] R. Ramlau and J. Niebsch, "Imbalance estimation without test masses for wind turbines," *Journal of Solar Energy Engineering*, vol. 131, no. 1, article 011010, 2009.

[19] Y. A. Khulief, M. A. Mohiuddin, and M. El-Gebeily, "A new method for field-balancing of high-speed flexible rotors without trial weights," *International Journal of Rotating Machinery*, vol. 2014, Article ID 603241, 11 pages, 2014.

[20] X. Li, L. Zheng, and Z. Liu, "Balancing of flexible rotors without trial weights based on finite element modal analysis," *Journal of Vibration and Control*, vol. 19, no. 3, pp. 461–470, 2012.

[21] J. V. D. Vegte and R. T. Lake, "Balancing of rotating systems during operation," *Journal of Sound and Vibration*, vol. 57, no. 2, pp. 225–235, 1978.

[22] B. Hredzak and G. Guo, "New electromechanical balancing device for active imbalance compensation," *Journal of Sound and Vibration*, vol. 294, no. 4-5, pp. 737–751, 2006.

[23] J. D. Moon, B. S. Kim, and S. H. Lee, "Development of the active balancing device for high-speed spindle system using influence coefficients," *International Journal of Machine Tools and Manufacture*, vol. 46, no. 9, pp. 978–987, 2006.

[24] K. Nakamoto, K. Adachi, and K. Shirase, "Proposal of real-time balancing mechanism using magnetic fluid for machine tool spindle," in *Manufacturing Systems and Technologies for the New Frontier*, pp. 387–390, Springer, London, UK, 2008.

[25] H. Fan, M. Jing, R. Wang, H. Liu, and J. Zhi, "New electromagnetic ring balancer for active imbalance compensation of rotating machinery," *Journal of Sound and Vibration*, vol. 333, no. 17, pp. 3837–3858, 2014.

[26] H. D. Nelson and J. M. McVaugh, "The dynamics of rotor bearing systems using finite elements," *Journal of Engineering for Industry*, vol. 98, no. 2, p. 593, 1976.

[27] H. D. Nelson, "A finite rotating shaft element using timoshenko beam theory," *Journal of Mechanical Design*, vol. 102, no. 4, p. 793, 1980.

[28] M. A. Mohiuddin and Y. A. Khulief, "Coupled bending torsional vibration of rotors using finite element," *Journal of Sound and Vibration*, vol. 223, no. 2, pp. 297–316, 1999.

[29] S. Lim, "Finite element analysis of flexural vibrations in hard disk drive spindle systems," *Journal of Sound and Vibration*, vol. 233, no. 4, pp. 597–612, 2000.

[30] J. Liu and Y. Shao, "Dynamic modeling for rigid rotor bearing systems with a localized defect considering additional deformations at the sharp edges," *Journal of Sound and Vibration*, vol. 398, pp. 84–102, 2017.

[31] L. H. Larsson and A. S. Douglas, *Elastic-Plastic Fracture Mechanics*, MIR Publishers, Moscow, Russia, 1978.

[32] M. Tsutsumi, M. Ohya, T. Aoyama, S. Shimizu, and S. Hachiga, "Deformation and interface pressure distribution of 1/10 tapered joints at high rotation speed," *International Journal of the Japan Society for Precision Engineering*, vol. 30, pp. 23–28, 1996.

[33] Y. H. Heo and K. J. Kim, "Definitions of non-stationary vibration power for time–frequency analysis and computational algorithms based upon harmonic wavelet transform," *Journal of Sound and Vibration*, vol. 336, no. 336, pp. 275–292, 2015.